CHAPTER

Experimental models of coarse-clast transport by tsunamis

27

Jan Oetjen[1], **Holger Schüttrumpf**[1], **Max Engel**[2,3]

[1]*Institute of Hydraulic Engineering and Water Resources Management, RWTH Aachen University, Aachen, Germany;* [2]*Institute of Geography, Heidelberg University, Heidelberg, Germany;* [3]*Geological Survey of Belgium, OD Earth and History of Life, Royal Belgian Institute of Natural Sciences, Brussels, Belgium*

Abstract

This chapter summarizes background and setup of wave-flume experiments investigating boulder transport by tsunamis. It emphasizes both opportunities for better understanding boulder transport in natural settings and limitations, i.e., the sources of uncertainty, related to these experiments. It also reviews the most important findings published so far, explains linkages with numerical models, and draws conclusions on research directions and open questions, which need to be tackled in future studies.

Keywords: Boulder; Experiments; Hydrodynamic; Scaling; Tsunami; Wave tank.

Introduction

Physical experiments are, beside in situ observations and theoretical analysis, the foundation of our understanding of how coastal coarse clasts (boulder- and block-sized) are transported by tsunamis and how to differentiate whether they were transported by storm waves or tsunamis. They provide clues to the development of empirical equations and numerical models describing the transport processes and fundamental mechanics (see Chapters 28 and 29). Rooted in pioneering tank models on the interaction of waves and clastic sediments, such as those of Bagnold (1940) simulating pebble beach formation, experiments focusing on the interaction of tsunamis and coarse clasts are a comparably young field with only a few well-documented examples (e.g., Imamura et al., 2008; Nandasena and Tanaka, 2013; Bressan et al., 2018).

Experiments on tsunami-induced boulder transport can be conducted in a well controllable and (in the optimal case) repeatable environment—in most cases a wave flume or wave basin—and, therefore, provide quantitative data on the governing parameters of boulder transport. However, an approximation to natural settings and downscaling of models in the lab is associated with several shortcomings such as inappropriate replication of bottom roughness, flow turbulences and trapped air in the flow (especially during the bore impact), or simplified topographies and boulder shapes.

Geological Records of Tsunamis and Other Extreme Waves. https://doi.org/10.1016/B978-0-12-815686-5.00027-4

This chapter presents typical experimental setups of wave-flume experiments on tsunami-induced boulder transport. It introduces the most important theoretical background for flume experiments and commonly applied measurement and wave-generation techniques and methods. Furthermore, the chapter reviews the most important findings published so far and explains the linkage between physical experiments and numerical models for boulder transport by tsunamis. It concludes with future research directions and open questions. While there are similar experimental studies on coastal boulder transport by storm waves (Hansom et al., 2008; Cytrynbaum, 2018; Cox et al., 2019), these are not systematically covered and considered beyond the scope of this review due to their significantly different hydrodynamics.

Dimensionless quantities and scaling of experiments

Dimensional analysis

Physical experiments regarding tsunami-induced boulder transport are typically conducted in a downscaled environment. The downscaling process is not straightforward, since important physical laws react sensitively toward changing dimensions, exemplified by the surface tension of water: a small pebble hitting the surface of a filled coffee cup only induces small uniform, circular waves on the water surface without strong turbulences or white water formation. In the same scenario with a 25 times larger "coffee cup" and "pebble," we observe turbulent flows around the impact resulting in locally high Froude numbers (Fr) with white water and distinct splashes.

To be able to describe fluid mechanics in a scaled environment properly, dimensional analysis (Kobus, 1974) is applied to find depending variables whose combination leads to a dimensionless quantity. These dimensionless variables can then be used for planning and optimizing scaled physical experiments and the proper transmission of their results to nature (Hughes, 1993; Martin and Pohl, 2000). Furthermore, dimensionless variables allow for reducing the number of variables, which need to be considered in experimental studies, since they are represented by depending key numbers (Hughes, 1993; Herwig, 2008). For experimental investigations of gravity-driven waves (like tsunamis), the Froude number is the most important variable and, thus, is derived in the following section as an example for dimensional analysis.

The Froude number and scaling laws

The Froude number

$$Fr = \frac{v}{\sqrt{g \cdot l}} [-] \tag{27.1}$$

(v [m/s] = velocity, g [m/s^2] = gravity and l [m] = characteristic length) expresses the ratio between gravity and inertia forces within the hydrodynamic system (Martin and Pohl, 2000). For the following example, it is important to recognize that every physical variable, e.g., the length $l = 10$ m, consists of a quantity (*10*), dimension (l), and unit (m). In principle, the scaling ratio for a variable in prototype and the scaled model is defined as follows:

$$M_x = \frac{x_P}{x_M} \tag{27.2}$$

where x stands for an arbitrary variable in the nature prototype (subscript P) or the scaled model (subscript M). However, for the dimensional analysis, some basic physical dimensions need to be defined as a ruling basis, which can rely, e.g., on electrical, thermal, or mechanical quantities (Goseberg, 2011). For hydrodynamic laboratory experiments with an open water surface and focusing on gravity-driven waves, a mechanical similarity between prototype and model is intended. Following this, the dimensional analysis is based on the following quantities: length in meter [m], time in seconds [s], and mass in kilogram [kg] (Martin and Pohl, 2000; Herwig, 2008; Goseberg, 2011).

Therefore, density ρ [kg/m^3], length l [m], volume V [m^3], time t [s], and acceleration a [m/s^2] are scaled as follows:

$$\text{Length} \quad M_l = \frac{l_P}{l_M} \tag{27.3}$$

$$\text{Density} \quad M_\rho = \frac{\rho_P}{\rho_M} \tag{27.4}$$

$$\text{Volume} \quad M_V = \frac{V_P}{V_M} = \frac{l_P^3}{l_M^3} = M_l^3 \tag{27.5}$$

$$\text{Time} \quad M_t = \frac{t_P}{t_M} \tag{27.6}$$

$$\text{Acceleration} \quad M_a = \frac{a_P}{a_M} = \frac{\frac{l_P}{t_P^2}}{\frac{l_P}{t_P^2}} = \frac{M_l}{M_t^2} \tag{27.7}$$

Scaling of the inertia or gravity forces:

$$\text{Inertia}: \quad \frac{F_{\mathrm{TP}}}{F_{\mathrm{TM}}} = \frac{\rho_P \cdot V_P \cdot a_P}{\rho_M \cdot V_M \cdot a_M} \tag{27.8}$$

$$\text{Gravity}: \quad \frac{F_{\mathrm{GP}}}{F_{\mathrm{GM}}} = \frac{\rho_P \cdot V_P \cdot g_P}{\rho_M \cdot V_M \cdot g_M} \tag{27.9}$$

Considering Eqs. (27.3) to (27.7), Eqs. (27.8) and (27.9) can be rewritten as shown:

$$M_T = \frac{F_{\mathrm{TP}}}{F_{\mathrm{TM}}} = \frac{\rho_P \cdot V_P \cdot a_P}{\rho_M \cdot V_M \cdot a_M} = \frac{M_\rho \cdot M_l^4}{M_t^2} \tag{27.10}$$

$$M_G = \frac{F_{\mathrm{GP}}}{F_{\mathrm{GM}}} = \frac{\rho_P \cdot V_P \cdot g_P}{\rho_M \cdot V_M \cdot g_M} = M_\rho \cdot M_g \cdot M_l^3 \tag{27.11}$$

Equalizing the scale numbers of two dominant forces leads to dimensionless key numbers and specified relationships, which allow converting the physical quantities between prototype and model (Martin and Pohl, 2000). In Froude-scaled models, the dominant forces are inertia and gravity. Therefore,

$$M_T = M_G \tag{27.12}$$

or, considering Eqs. (27.10) and (27.11),

$$\frac{M_\rho \cdot M_l^4}{M_t^2} = M_\rho \cdot M_g \cdot M_l^3 \tag{27.13}$$

Laboratory experiments are generally conducted by using freshwater. The slightly lower density of freshwater (approximately 2.7% below saltwater in a temperature of 25°C) is usually neglected in such experiments. Therefore, density and gravity remain the same in prototype and model, and lead, by considering Eq. (27.13), to the following scaling rule for the time ratio M_t (considering the length ratio or geometric similarity, respectively, as the leading constant) in Froude models:

$$M_t = \sqrt{M_l} \tag{27.14}$$

Rewriting, extending with $\frac{\mathrm{M_l}}{\mathrm{M_l}}$ and substituting with $M_t^2 = M_l$ (Eq. 27.13) results in

$$1 = \frac{M_l}{M_t^2 \cdot M_g} = \frac{M_l}{M_t^2 \cdot M_g} \cdot \frac{M_l}{M_l} = \frac{M_l^2}{M_t^2 \cdot M_g \cdot M_l} = \frac{M_l^2}{M_t^2 \cdot M_g \cdot M_t^2} = \frac{M_v^2}{M_g \cdot M_l} \tag{27.15}$$

which becomes

$$1 = \frac{\frac{v_P^2}{v_M^2}}{\frac{g_P}{g_M} \cdot \frac{l_P}{l_M}} \tag{27.16}$$

or

$$Fr_P = \frac{v_P}{\sqrt{g \cdot l_P}} = \frac{v_M}{\sqrt{g \cdot l_M}} = Fr_M \tag{27.17}$$

ensuring that the Froude number is equal in prototype and model. This dimensional analysis is focused on mechanically driven Froude models and can be carried out for every depending variable set (Gibbings, 2011). Further explanations and examples are provided by Buckingham (1914), Hughes (1993), or Martin and Pohl (2000).

The example for a dimensional analysis regarding the Froude number already shows the scaling law for time in Eq. (27.14). To account for further scaling effects, mechanical scaling laws are introduced, in hydrodynamics determined by the geometric (shape, $\boldsymbol{\lambda}$ [−]), kinematic (motion, $\boldsymbol{\tau}$ [−]), and dynamic (forces, $\boldsymbol{\kappa}$ [−]) similarity between prototype and model. In most cases the geometric similarity is the leading constant that determines the size of the model following:

$$\text{Geometric similarity} \quad \lambda = \frac{l_P}{l_M} \tag{27.18}$$

$$\text{Kinematic similarity} \quad \tau = \frac{t_P}{t_M} \tag{27.19}$$

$$\text{Dynamic similarity} \quad \kappa = \frac{F_P}{F_M} \tag{27.20}$$

with l [m] for length or geometric dimension, t [s] for time, and F [N] for force. To keep the ratio for the dynamic similarity true for hydrodynamic experiments, the acting forces for inertia, gravity, friction, surface, and spring (elastic) force need to be considered. The similarity laws for these forces depend, with varying power, on the geometric ratio between prototype and model. Additionally, inertia and friction forces are influenced by the time ratio between prototype and model. Therefore, to keep a complete similarity for the dynamic forces, the following equation (Eq. 27.21) needs to be fulfilled:

$$\kappa_{\text{inertia}} = \kappa_{\text{gravity}} = \kappa_{\text{friction}} = \kappa_{\text{surface forces}} = \kappa_{\text{elasticity}} \tag{27.21}$$

$$\kappa_{\text{inertia}} = \frac{\rho_P}{\rho_M} \cdot \frac{\lambda^4}{\tau^2}, \tag{27.22}$$

$$\kappa_{\text{gravity}} = \frac{\rho_P}{\rho_M} \cdot \lambda^3, \tag{27.23}$$

$$\kappa_{\text{friction}} = \frac{\eta_P}{\eta_M} \cdot \frac{\lambda^2}{\tau}, \tag{27.24}$$

$$\kappa_{\text{surface forces}} = \frac{\sigma_P}{\sigma_M} \cdot \lambda, \tag{27.25}$$

$$\kappa_{\text{elasticity}} = \frac{E_P}{E_M} \cdot \lambda^2, \tag{27.26}$$

$$\kappa = \frac{\rho_P}{\rho_M} \cdot \frac{\lambda^4}{\tau^2} = \frac{\rho_P}{\rho_M} \cdot \lambda^3 = \frac{\eta_P}{\eta_M} \cdot \frac{\lambda^2}{\tau} = \frac{\sigma_P}{\sigma_M} \cdot \lambda = \frac{E_P}{E_M} \cdot \lambda^2 \tag{27.27}$$

with ρ for density [kg/m^3], λ as the length ratio between prototype and model, τ as the time ratio [-], E [N/m^2] for elasticity, η [N • t/m^2] for dynamic viscosity, and σ [N/m] for surface tension.

Assuming that the investigated medium is the same in prototype and model ($\rho_P = \rho_M$), which is true for water-related experiments, Eq. (27.27) can be simplified to this:

$$\kappa = \frac{\lambda^4}{\tau^2} = \lambda^3 = \frac{\lambda^2}{\tau} = \lambda = \lambda^2 \tag{27.28}$$

To keep full similarity between prototype and model, Eq. (27.29)

$$\kappa = \tau = \lambda \tag{27.29}$$

has to be fulfilled, which obviously is not possible with Eq. (27.28), except for a scale of 1:1. Thus, only the two most important forces are commonly considered in scaled laboratory experiments to keep the geometric ratio (almost) free of choice. Mainly four scaling laws are available for this issue, each focusing on the similarity of two specific force types (Martin and Pohl, 2000).

For laboratory experiments on boulder transport by tsunamis, the Froude scaling law is the appropriate equation since the impact of a hydraulic bore is mainly gravity-driven (Robertson et al., 2011; Lloyd, 2016; Li and Chanson, 2017). In experiments scaled according to the Froude scaling law, the Froude number is the same both for the prototype and for the model:

$$Fr_P = \frac{v_P}{\sqrt{g \cdot l_P}} = \frac{v_M}{\sqrt{g \cdot l_M}} = Fr_M \tag{27.30}$$

It keeps the similarity between inertia and gravity forces (holding a constant Froude number), which are the most influencing forces in gravity-driven, free-surface flows, i.e., tsunami waves. Table 27.1 shows the most important relationships, which need to be considered while planning an experimental hydrodynamic/hydraulic model following the Froude scaling law.

If possible, Froude-scaled experiments should not be carried out in the transition zone between subcritical and supercritical flows ($Fr \approx 1$), as the flow could easily flip between both states caused by small divergences, e.g., in bottom roughness.

Table 27.1 Froude scaling laws.

Parameter	Sign	Dimension	Scaling law	
Length	l	[m]	$l_M = \frac{l_P}{\lambda}; \lambda = \frac{l_P}{l_M}$	(31)
Area	A	[m^2]	$A_M = \frac{A_P}{\lambda^2}$	(32)
Volume	V	[m^3]	$V_M = \frac{V_P}{\lambda^3}$	(33)
Time	t	[s]	$t_M = \frac{t_P}{\sqrt{\lambda}}$	(34)
Velocity	v	[m/s]	$v_M = \frac{v_P}{\sqrt{\lambda}}$	(35)
Acceleration	a	[m/s^2]	$a_M = a_P$	(36)
Force	F	[N]	$F_M = \frac{F_P}{\lambda^3}$	(37)

Scaling effects regarding turbulence and air inclusions in the bore tip need to be considered even more carefully in Froude-scaled experiments since these are not properly scalable (She and Leveque, 1994; Chanson, 2009; Nistor et al., 2017).

Further restrictions regarding downscaling arise from possible transitions from turbulent to laminar flow conditions (denoted by the dimensionless Reynolds number *Re*, see Section The Reynolds number). However, recognizing and considering the Froude scaling law and the influence of the Reynolds number in laboratory experiments does not allow for scaling as geometrically small as possible (e.g., due to surface tension of water). A minimum flow depth of 2 cm should be realized in the model to avoid the influence of surface tension on wave propagation, for example (Le Méhauté, 1976).

The Reynolds number

If laboratory experiments are Froude-scaled, the Froude number is conserved between the prototype and model, as explained earlier. However, beside the Froude number, the influence of the Reynolds number

$$\mathrm{Re} = \frac{\rho \cdot v \cdot d}{\eta} [-] \tag{27.38}$$

with ρ [kg/m^3] as the fluid density, v [m/s] as the fluid velocity, d [m] as the characteristic length (e.g., flow depth or boulder diameter), and η [kg/(m·s)] as dynamic viscosity, needs to be considered when conducting experiments related to boulder transport by tsunamis. The Reynolds number describes the ratio between inertia and viscous forces and indicates (but does not prove) the type of flow in terms of laminar (low Reynolds number) or turbulent (generally high Reynolds number) flow (Fig. 27.1). Froude scaling of natural prototypes with only gentle turbulent flows could result in laminar conditions in the model due to the lower flow velocity in the downscaled environment inadequately representing the processes in nature (Martin and Pohl, 2000). Therefore, the Reynolds number of the model should be compared to the *transition Reynolds number* (Re_{crit}), which describes the threshold from turbulent to laminar flows (e.g., $Re_{crit} \approx 2320$ for flow in a pipe), while planning physical hydrodynamic experiments (Martin and Pohl, 2000). Since tsunami runup is typically highly turbulent (Yeh, 1991), laboratory experiments following Froude scaling laws require a similar turbulent flow regime, even if the Reynolds number cannot be conserved between the prototype and model due to Froude scaling.

Moreover, a high Reynolds number ensures that inertial forces are dominating in the experimental setup compared to the viscous forces, which is an important property regarding the influence of boundary roughness. Since the active friction is a function of fluid viscosity and boundary roughness, scaling of the roughness might result in violating the threshold from rough to smooth hydraulic conditions (or vice versa) and cause an unintended change in the influence of boundary roughness on flow conditions (Martin and Pohl, 2000). Generally, reducing the boundary

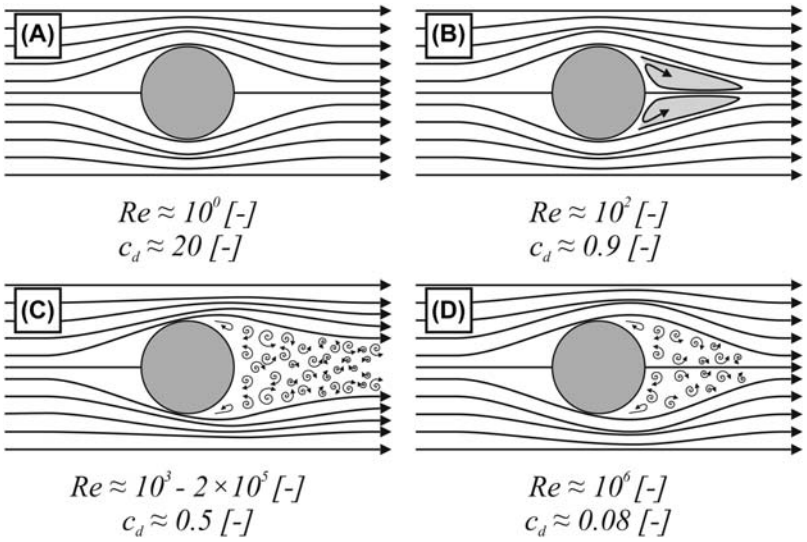

FIGURE 27.1

Streamlines around a smooth sphere by different Reynolds numbers. The drag coefficient decreases from (A) to (D). (A) Low Reynolds number. Inertial forces are much lower than viscous force along the sphere. (B) With increasing Reynolds number, the stream is detached and stationary eddies occur behind the sphere. (C) Higher Reynolds number. The eddies behind the boulder increase until instabilities initiate their detachment and lead to a broad turbulent stream behind the boulder. The drag coefficient is fairly constant in this range. (D) Very high Reynolds number. Comparable to (C) but with narrower turbulent stream behind the sphere.

roughness while ignoring the geometric similarity can help to avoid unintended changes in the hydraulic friction conditions (Heller, 2011). However, if the hydraulic conditions in the natural prototype are already close to the threshold from hydraulic-rough to hydraulic-smooth, applying a fluid of adjusted viscosity or operating a distorted (e.g., superelevated) model should be considered (Martin and Pohl, 2000).

Furthermore, when focusing on tsunami−boulder interaction, the nonlinear influence of the Reynolds number on the shape-specific drag coefficient c_d [-] should be considered. The drag coefficient is an experimentally derived and *Re*-depending (Spurk and Aksel, 2018), dimensionless number describing the resistance of an object to the surrounding flow (e.g., the tsunami runup) and influences the force of drag directly following:

$$F_d = \frac{1}{2} \cdot \rho \cdot v^2 \cdot c_d \cdot A[N] \tag{27.39}$$

where v [m/s] is the flow velocity relative to the fluid, and A [m^2] is the reference area of the object (commonly the frontal area of the object). The higher the drag coefficient of a particular body, the more force is exerted to the exposed object during

the flow impact. Therefore, the coefficient of drag and, thus, the Reynolds number, have a strong influence on the transport of boulder by tsunamis. To keep the coefficient of drag of the transported body in the range of natural prototypes, the Reynolds number needs to be in the same range even if it is not possible to conserve the exact value between prototype and model (Munson et al., 2009; e.g., in the range of $Re = 10^3$ [-] to $Re = 2 \times 10^5$ [-] for sphere, compare Fig. 27.1). Nevertheless, for setups of high Reynolds numbers and bodies different from smooth spheres, the drag coefficient becomes essentially independent from the Reynolds number (Munson et al., 2009).

As shown before, it is not possible to keep the Reynolds number the same between prototype and model if the model is scaled following Froude scaling laws. Reference values for Reynolds numbers for some idealized boulder models in laboratory boulder transport experiments can be found in Bressan et al. (2018) or Nandasena and Tanaka (2013). Further advice concerning scaling effects and corresponding issues can be found in Martin and Pohl (2000) or Fang (2019). Heller (2011) provides further rules, hints, and examples to deal with scaling effects for several experimental hydrodynamic setups.

Measuring approaches in the wave tank

The reliability of information derived from physical experiments is also closely linked to the recording, usage, and interpretation of data. A broad range of measurement devices is available and chosen based on study goals, parameters of interest (e.g., mobilization threshold or transport distance), availability of measurement devices and time for collecting, processing and interpretation of data. It is recommended to focus on a few crucial parameters only and to consider extending the study in the case that more time is available or the experiments show unexpected results.

Measuring the wave behavior and parameters is an essential component of physical hydraulic experiments. For wave measurements, the choice and final placement of devices in the flume as well as the subsequent data analysis need to be planned carefully.

Ultrasonic wave gauges can be a basis for measuring the wave development during the impact on the boulder and runup. However, at least in a wave basin, these are point measurements of a three-dimensional phenomenon. Therefore, if the focus of the experiments is to particularly investigate the wave behavior, the use of 3D measurement systems might be an option (e.g., Evers, 2018).

Propeller velocimeters are often used to measure current or wave velocity, since they are comparably easy to install and use. However, since measurements are based on revolutions of the propeller per time, inaccuracies occur at the first wave impact (propeller needs time to reach full speed). Furthermore, they suffer from small particles affecting the rotation mechanics leading to breakage and measurement errors. Other options for velocity measurements are acoustic doppler velocimetry, electromagnetic liquid velocity meters, laser measurements, particle-image velocimetry, and electromagnetic current meters, as described in more detail by Martin and Pohl (2000) or Tavoularis (2006).

Investigations of the boulder transport path benefit from the use of an inertial measurement unit (IMU) or a real-time locating system installed inside the boulder replicate (e.g., Gronz et al., 2016; Nistor et al., 2017), which records parameters such as acceleration, direction and duration of motion, or altitude. IMUs, however, can be influenced by electronic waves of other instruments in the laboratory and alter the center of mass and, thus, the behavior of the boulder. Another alternative is the use of high-speed camera recordings in combination with a grid applied on the model's surface or to combine both approaches. Video analysis requires automated distance measurements for each recorded frame, which take surface inclinations of the model into account (e.g., by using MATLAB scripts; Stolle et al., 2016). Multiple camera positions (e.g., side and top view) are recommended to compensate for white-water disturbances. Fig. 27.2 shows an automatized color range-based boulder-tracking algorithm developed in MATLAB. It can be seen that the algorithm is affected by colors similar to the boulder color (white water, white lines). While white water remains problematic, disturbances can be avoided by using clearly contrasting colors. Furthermore, applying an algorithm based solely on color ranges remains a very simple approach. Applying algorithms accounting for neighboring pixel or applying more sophisticated filters (e.g., Kalman Filter in Stolle et al., 2016) could lead to significantly better results.

Types of wave generation

Several approaches exist for wave generation. They range from relatively simple techniques for tsunami bores (e.g., dam-break scenarios; Imamura et al., 2008; Nandasena and Tanaka, 2013; Freund, 2014; Liu et al., 2015; Bressan et al., 2018), which are most commonly used in experiments addressing tsunami-induced boulder transport, to more sophisticated techniques with wave paddles or pumps resembling a desired wave series (e.g., Goseberg et al., 2016; Schimmels et al., 2016).

In the dam-break scenario, the tsunami is not modeled as a solitary wave but as a nearshore and already broken tsunami of highly turbulent flow with a high Reynolds number (Fig. 27.3). The tsunami bore is based on the sudden release of a specific amount of water stored behind a gate (slide- or swivel-type valve), which is either opened manually by hand (Bressan et al., 2018), by a pulley system (Liu et al., 2017), or by a pneumatic mechanism (Hsu et al., 2012). For long waves, i.e., the unbroken tsunami, a piston-type wave maker is often applied, where pistons displace the water column of a connected tank in horizontal direction (Fig. 27.3). Piston-type wave makers can also be installed as multiple devices arranged in a wave basin (e.g., Rhinefrank et al., 2010).

Furthermore, the tsunami or bore generation can be based on pumping systems of different types. In Oetjen et al. (2017, 2018), the bore is generated by pumping water through a rectifier on a dry bed, where the water runs against a barrier of a specific height, which generates the final bore (Fig. 27.4). High-end pump and pneumatic systems such as in Goseberg (2011, 2012), or the HR Wallingford/UCL Tsunami

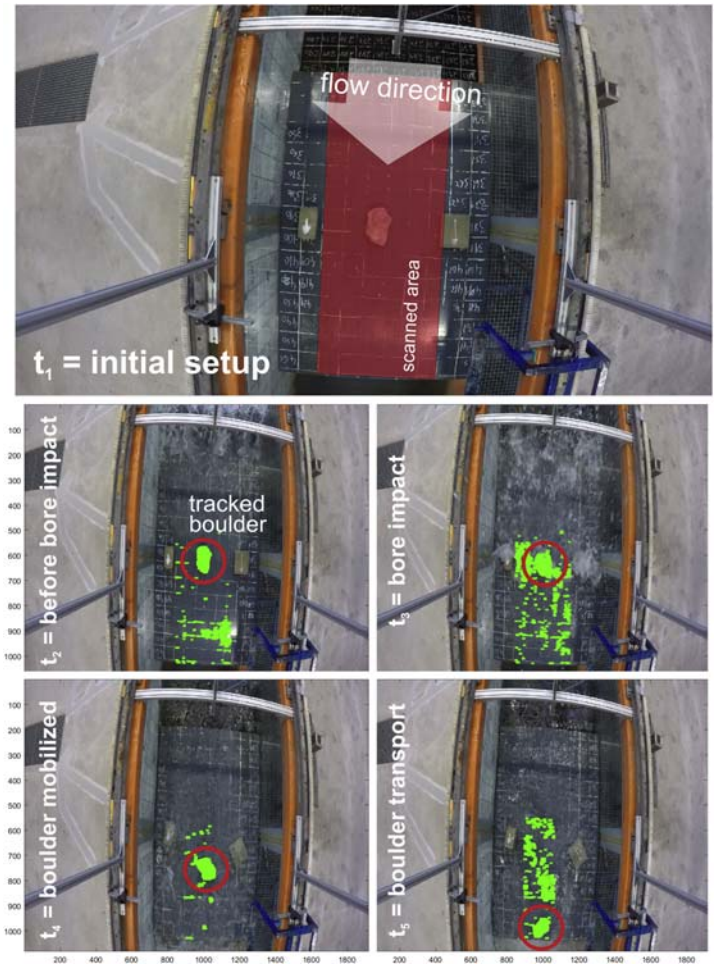

FIGURE 27.2

Boulder tracking algorithm developed in MATLAB. Image on top shows the initial state. Here, the boulder is detected by specifying rgb color ranges encompassing only the boulder color by excluding others. Time steps 2 to 5 show the detection shortcomings especially due to the occurrence of white water, the color of which is too similar.

Generator (Allsop et al., 2014), provide more control on the bore in terms of wavelength, height, etc. (Fig. 27.4). Goseberg (2011, 2012) developed an advanced mechanism for the generation of long waves based on pumps, which allows controlling the discharge using a predefined wave-generation algorithm. Here, the long wave is generated by adjusting acceleration and deceleration phases (positive and negative pumping phase) of the water column to generate wave crests and wave troughs. In Allsop et al. (2014), the wave is generated as a pump-driven dam- break scenario.

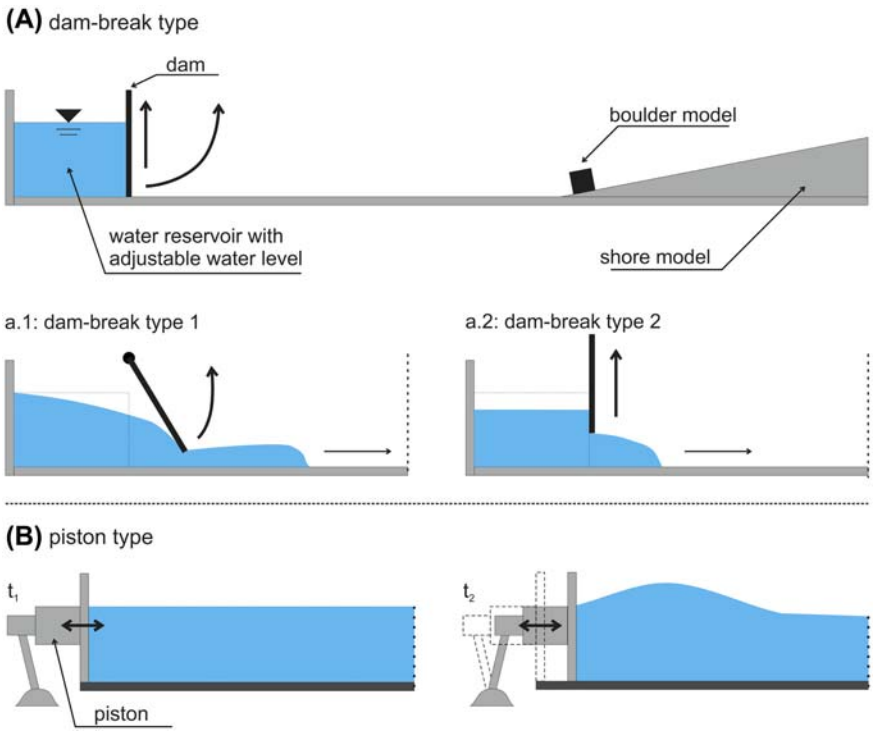

FIGURE 27.3

Dam-break and piston mechanism for bore generation. In dam-break setups the bore is generated by suddenly opening a gate and the subsequent water release from an impounded storage (A). In piston-type setups (B) the wave is generated by accelerating and releasing the water column horizontally using a piston-driven paddle.

However, by generating the wave through a controllable tank in which several water depths and release velocities can be realized, the Tsunami Generator allows creating more specific wave shapes of desired heights and velocities (Fig. 27.3). A significant advantage of computer-controlled systems as in Goseberg (2011, 2012), Goseberg et al. (2013), Oetjen et al. (2017, 2018), or Nistor et al. (2017) is an enhanced reproducibility.

Parameters studied in physical experiments

Typical parameters investigated in experiments on tsunami boulder transport (e.g., Imamura et al., 2008; Nandasena and Tanaka, 2013; Liu et al., 2015; Oetjen et al., 2017; Bressan et al., 2018) are the initial boulder setting (submerged, partially submerged, subaerial), wave parameters (velocity, height), orientation of the main boulder axis to the flow (0 degrees, 45 degrees, 90 degrees) (Fig. 27.4), and boulder

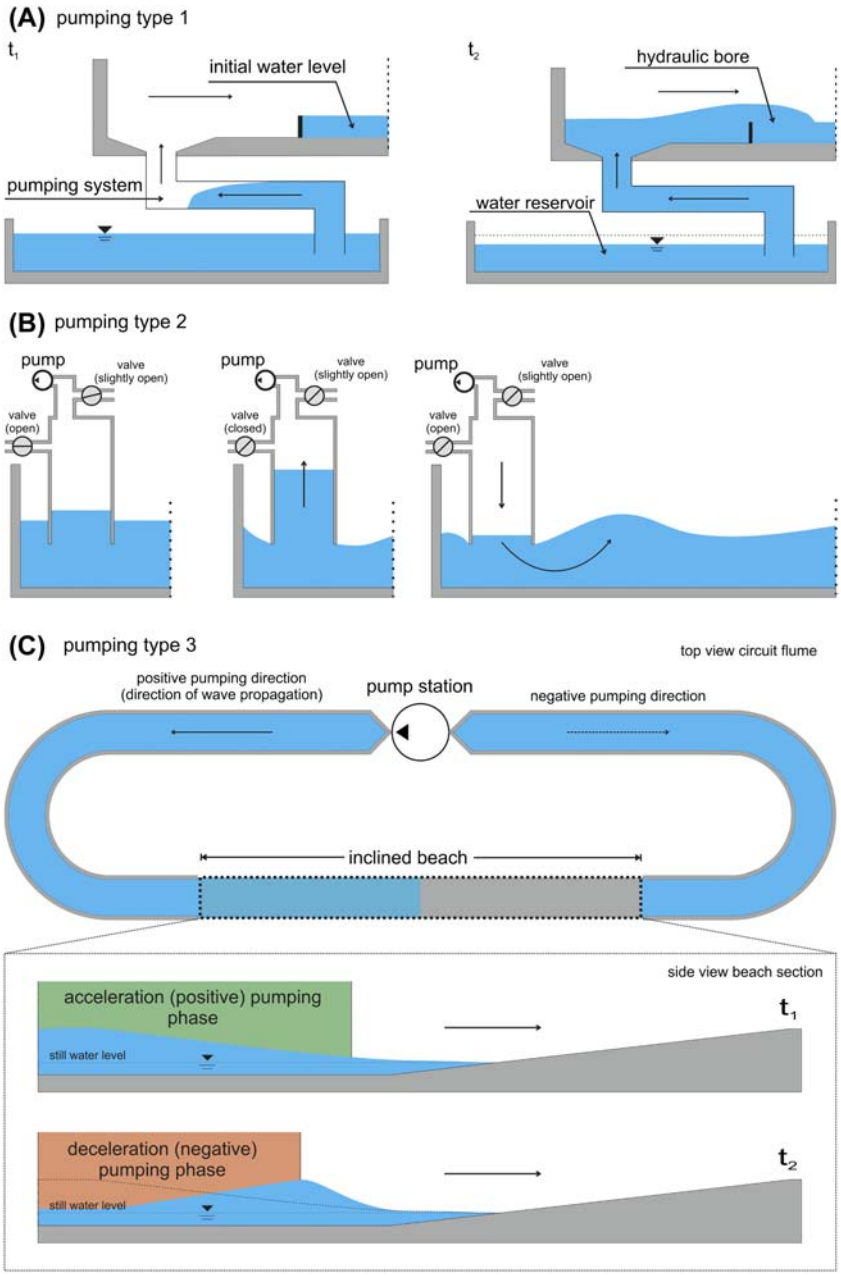

FIGURE 27.4

Pumping-type wave maker modified after (A) Oetjen et al. (2017): bore generation by pumping water out from a reservoir vertically and subsequent gravity-driven flow over an

shape (cubic, natural, flat). In most existing studies, the shore is kept constant and designed as a uniformly inclined shore with angles between 5 degrees and 12 degrees (e.g., Nandasena and Tanaka, 2013; Liu et al., 2015; Bressan et al., 2018). With the number of varied parameters, the number of experimental runs hugely increases, following the equation

$$Number\ of\ necessary\ runs = \prod_{i}^{n} P_i \tag{27.40}$$

where P_i = the number of variations for the parameter i. Thus, investigating three types of pre-transport setting (submerged, partially submerged, subaerial), three types of main axis orientation (0 degrees, 45 degrees, 90 degrees), and two different shapes, the minimum number of runs is 18. Since experimental runs are commonly repeated at least three times, the preceding example results in 54 runs.

The parameters control boulder transport in many different ways. Altering the boulder shape in terms of flatness or cuboid/spherical shapes changes the available impact area for the incoming wave. The force transferred from the wave to the boulder decreases with a more streamline boulder shape. On the other hand, a streamlined boulder shape with a natural, rough surface increases the energy transfer, which is translated to transport capacity. The orientation of the boulder to the flow influences the energy transfer in a similar way; the long axis aligned perpendicular to the flow captures more wave energy. In agreement with field observations (e.g., May et al., 2015; Boesl et al., 2019), several experiments showed that boulders tend to rotate around their main axis perpendicular to the flow immediately after the wave impact (e.g., Imamura et al., 2008). During this process, energy is dissipated and no longer available for transport. Changing the bottom roughness during the experiments provides information on the resisting force resulting from bottom friction. Table 27.2 provides a summary of the most commonly investigated parameters, their influence on boulder transport, and finally the estimated complexity of the investigation.

Published wave-tank experiments on tsunami-boulder transport

Experimental setups

Experiments have been conducted with boulders of several shapes, dimensions and densities. The dimensions range between main axis lengths of <2 cm up to 15 cm and densities between 1.5 g/cm^3 to 2.71 g/cm^3. Generally, the boulder dimensions

installed barrier; (B) HR Wallingford (Allsop et al., 2014): wave generation by suctioning and releasing water vertically; and (C) Goseberg (2011): accelerating and decelerating the water column by pumping water either in positive or negative direction in a looped channel.

Table 27.2 Examples for parameters of interest in physical experiments and their influence. A qualitative evaluation is given on the necessary effort to implement parameter changes in the model setup.

	Direct influence on								
Parameter	**Impact force**	**Duration of impact**	**Available wave impact area**	**Active friction**	**Resisting force**	**Available wave energy**	**Available transport path**	**Impact force over time**	**Level of complexity to investigate**
Wave parameter (velocity, height, shape)	X	X				X			Easy to difficult (depending on wave-making mechanism)
Boulder shape			X	X				X	Medium
Boulder density/ weight				X	X				Medium
Boulder orientation			X		X			X	Easy
Bottom roughness					X	X			Difficult
Submergence			X			X		X	Easy
Shore type/ shape			X		X	X	X	X	Medium

depend on the focus of the study and on the applied scale. However, most boulder experiments do not follow a natural prototype setting. To characterize the shape of boulder models, Nandasena and Tanaka (2013) introduce the "flatness index" (FI) for their experiments, which accounts for the ratio between the boulder axes following the equation

$$FI = \frac{a+b}{2 \cdot c} \tag{27.41}$$

with a [cm], b [cm], and c [cm] for the boulders' long, intermediate, and short (height) axes.

Experimental setups of the most relevant published studies are summarized in Table 27.3 and Figs. 27.6 and 27.7. In a further study not yet published internationally, Freund (2014) investigates six different cuboid boulders of $8 \times 6 \times 3$ cm^3 (FI = 2.33) and $5 \times 5 \times 5$ cm^3 (FI = 1) with densities of 1.98 g/cm^3, 2.4 g/cm^3, and 3.1 g/cm^3, respectively. Freund (2014) uses a 19.05 m long, 0.3 m wide, and 0.35 m high flume in combination with a dam-break mechanism and a shore inclination of 1:20. The author compares different degrees of pre-transport submergence from subaerial over partially submerged to fully submerged. In the same laboratory, Strusińska-Correira et al. (2017) study tsunami-induced boulder transport using two different boulder shapes (cubic and cuboids) made of concrete (density $\rho = 2.1$ g/cm^3) with axis dimension ranging from $a = 16$–44 cm, $b = 16$–22 cm, and $c = 8$–22 cm. An initial water depth of 0.6 m is used in the flume.

Key findings

Nandasena and Tanaka (2013) find different predominant transport modes depending on boulder shape. While their rather flat boulders (FI ~2–3) mainly slide, boulders of a lower FI of ~1 tend to roll. Imamura et al. (2008), however, do not indicate varying transport modes even though the FI of their boulder models also ranges between 1 and 2. The correlation between transport mode and FI found by Nandasena and Tanaka (2013) indicates a highly sensitive boulder behavior even if dimensionless parameters are applied. Liu et al. (2015) observe rolling transport in only one case, whereas in all other experimental runs the boulder is transported by sliding, showing that the different scales in which the experiments are conducted are key to understand the diverging transport modes. Imamura et al. (2008) reach flow velocities of up to 1.5 m/s, which is comparable to the 1.4 m/s in Liu et al. (2015). However, Liu et al. (2015) use a boulder of $20 \times 12 \times 12$ cm^3, whereas the largest one of Imamura et al. (2008) measures $3.2 \times 3.2 \times 3.2$ cm^3, i.e., a ratio of 3.75:1 (Table 27.3). By applying the Froude scaling law, the velocity of Imamura et al. (2008) becomes the following:

$$\frac{v_P}{v_M} = \sqrt{\boldsymbol{\lambda}}$$

$$v_P = \sqrt{\boldsymbol{\lambda}} \cdot v_M$$

Table 27.3 Comparison of the experimental parameters from Imamura et al. (2008), Nandasena and Tanaka (2013), Liu et al. (2015), and Bressan et al. (2018).

			Nandasena and Tanaka (2013)	Imamura et al. (2008)	Bressan et al. (2018)	Liu et al. (2015)
Flume	Dimension	l [m]	18	10	11	18
		h [m]	0.75	n.p.	n.p.	n.p.
		w [m]	0.4	0.3	0.5	1
	Shore	[-]	Uniformly inclined (1:20)	Uniformly inclined (1:10)	Uniformly inclined (1:10)	Uniformly inclined (3.75:100)
	Initial water level [cm]		15	15	Dry bed	40
			20	20		42
			25	25		45
			30	30		-
Boulder	Number of different boulders		15	6	4	1
	Dimension [cm] (following the volume)	Min	1.5 × 1.5 × 1.5	1.6 × 1.6 × 1.6	3.05 × 3.00 × 2.85	20 × 12 × 12
		Max	8 × 4 × 4	3.2 × 3.2 × 3.2	5.92 × 3.14 × 3.08	
	Flatness index [-]		1–3	1–2	1.03–1.47	1.33
	Density [kg/m^3]	Min	1723*	1550	1900	2400
		Max	2880*	2710	2600	
	Orientation [°]		0	0	0	0
			45	-	45	45
			90	90	90	90

Continued

Table 27.3 Comparison of the experimental parameters from Imamura et al. (2008), Nandasena and Tanaka (2013), Liu et al. (2015), and Bressan et al. (2018).—*cont'd*

			Nandasena and Tanaka (2013)	Imamura et al. (2008)	Bressan et al. (2018)	Liu et al. (2015)
	Submergence		Subaerial	Partially submerged	Partially submerged (seems also subaerial and submerged. But not clearly published)	Subaerial
Bore generation	Wave vel. (app.) [m/s]		0.7–1.3	1.5	0.25	1.24–1.37
	Max. wave height (app.) [cm]		8.7–14.7	n.p.	n.p.	11.7–13.3
	Type		Dam break	Dam break	Dam break	Dam break
Key outcomes			Boulders with FI = 2 and 3 tend to sliding	Mainly rolling and saltating transportation for cubic boulder	Boulder experiments are highly uncertain	Sliding as predominant transport mode
			Boulders with FI = 1 tend to rolling			
			Transport mode is influenced by friction	Shorter transport distance for non-cubic block	Identification of three velocity zones regarding the possibility for boulder mobilization: certain boulder mobilization, maybe mobilization, impossible mobilization	Shorter total transport distance for rolling
			Impact force does not significantly influence the total transport distance			Transport distance is sensitive regarding the bore height/velocity
			Pre-transport angle influence the total transport distance significantly			Boulder transport can be divided in acceleration, steady, and deceleration phase

n.p.: not published;
**not clearly published whether measured dry or wet*

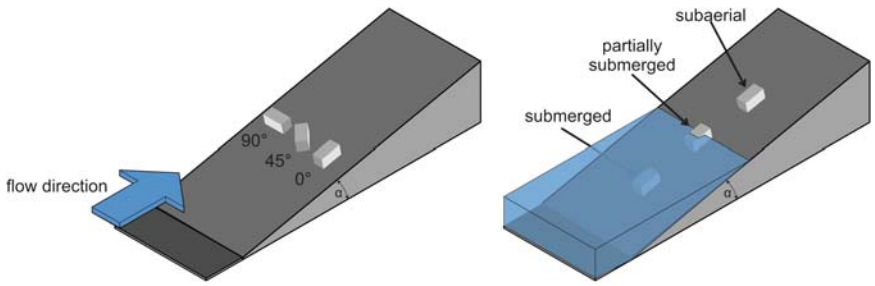

FIGURE 27.5

Typical boulder orientation and submergence in physical experiments.

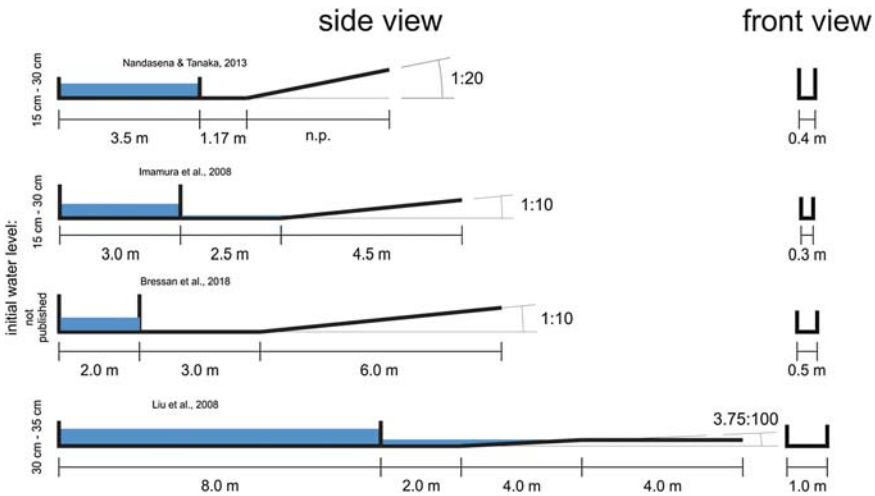

FIGURE 27.6

Comparison of the experimental flumes from Imamura et al. (2008), Nandasena and Tanaka (2013), Liu et al. (2015), and Bressan et al. (2018).

$$2.9\frac{m}{s} = \sqrt{3.75}\cdot 1.5\ \frac{m}{s}$$

$$v_{Imamura} = 2.9\frac{m}{s} \neq 1.4\frac{m}{s} = v_{Liu}$$

This example shows the relevance of appropriate scaling when comparing results of different experiments and labs (Table 27.4, Fig. 27.8).

Furthermore, Liu et al. (2015) report a time lag of 1 s between bore impact and boulder mobilization, which has not been reported by Imamura et al. (2008) and is attributed to the significantly larger wave height to boulder height ratio (Liu et al., 2015). Regarding incipient motion, Bressan et al. (2018) find that a boulder may start moving by the approaching bore even before it is completely submerged and that with decreasing flow depth a higher flow velocity is needed to mobilize the boulder.

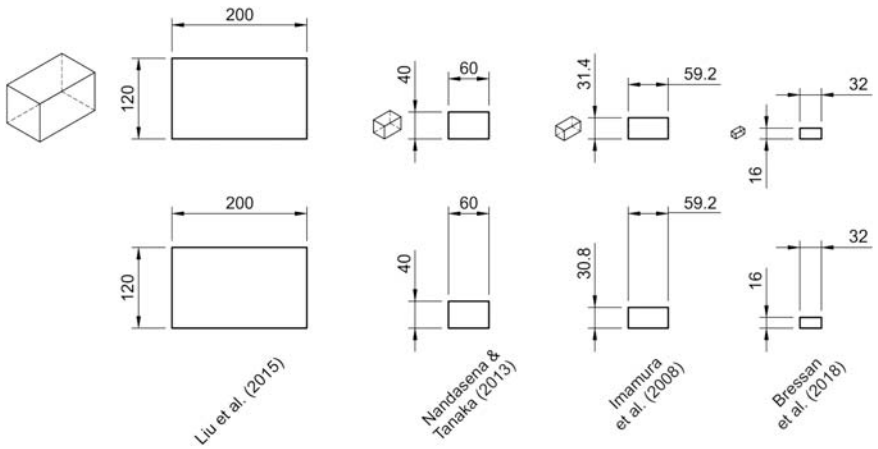

FIGURE 27.7

Comparison of the largest applied boulders (in mm) from Imamura et al. (2008), Nandasena and Tanaka (2013), Liu et al. (2015), and Bressan et al. (2018).

Maximum transport distance is strongly influenced by boulder orientation. Nandasena and Tanaka (2013) find a 27% shorter distance in case the main axis is oriented parallel to the flow and a 3% shorter distance for a 45-degree orientation. In a two-boulder setting, Nandasena and Tanaka (2013) find a slightly increased maximum transport distance for one boulder at the expense of the second one, attributed to momentum transfer during boulder-boulder collisions.

Bressan et al. (2018) identify flow turbulences to significantly influence the boulder behavior resulting in a widely scattered transport pattern. Thus, they recommend considering value ranges for flow depth and velocity instead of using exact values when reconstructing past boulder transport events. In general, the authors define three stages of transport: an acceleration phase, constant moving, and deceleration. Before the acceleration phase, a phase of beginning mobilization has been identified, in which the bore impacts the boulder but resisting forces are not exceeded and the boulder still rests. This phase can further be divided in velocity zones, where the boulder is certainly, maybe, or impossibly mobilized (Bressan et al., 2018).

Finally, Freund (2014) finds an increasing influence of the flow velocity on boulder transport with decreasing density of the boulder. The author observes that submerged boulders are mobilized after a short time lag when the bore impacts, whereas subaerial ones are immediately set in motion, mostly through sliding.

Further related studies

Besides the quasi two-dimensional studies on tsunami transport of Imamura et al. (2008), Nandasena and Tanaka (2013), Liu et al. (2015), and Bressan et al. (2018), other experiments focusing on similar hydrodynamic processes and environments also provide important implications (see also Table 27.5). Stolle et al. (2016)

Table 27.4 Scaled comparison (using scaling laws in previous sections.) between Imamura et al. (2008), Nandasena and Tanaka (2013), Liu et al. (2015), and Bressan et al. (2018). No further parameter (boulder dimension, weight, etc.) is considered. If available, the maximum velocity is taken for comparison. For Bressan et al. (2018), the calculated average velocity is used. From every calculation, one boulder is taken for comparison that is in a similar range for FI and density. As leading scaling parameter, the a-axis is considered.

	Boulder dimension					Scale to Liu et al. (2015)	Max bore velocity		Max. Transport distance	
	a	b	c	V	FI		$v_{original}$	v_{scaled}	$\Delta d_{original}$	Δd_{scaled}
	cm			cm^3	[-]	[-]	[m/s]		[cm]	
Liu et al. (2015)	20	12	12	2880	1.42	Reference	1.24	1.24	233	233
Nandasena and Tanaka (2013)	6	4	4	96	1.25	3.33	1.32	2.41	119	396
Imamura et al. (2008)	3.2	1.6	1.6	8.2	1.5	6.25	1.54	3.85	140	875
Bressan et al. (2018)	5.92	3.14	3.08	57.3	1.47	3.38	0.25	0.46	n/a	n/a

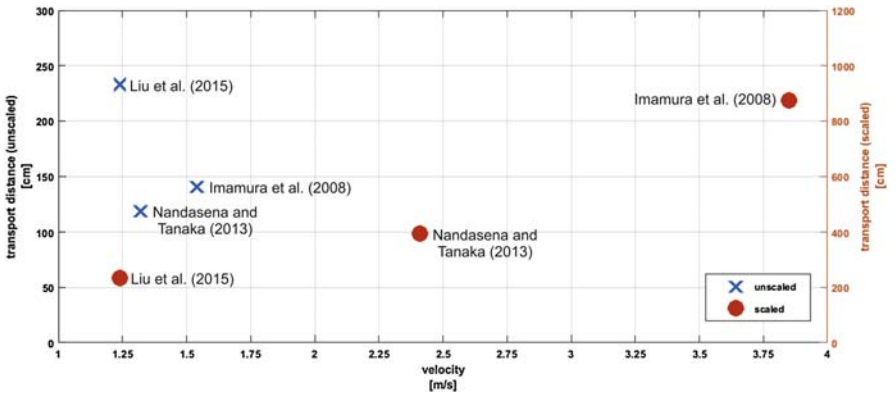

FIGURE 27.8

Graphic comparison of transport distances and flow velocities in Imamura et al. (2008), Nandasena and Tanaka (2013), and Liu et al. (2015) for scaled and unscaled results (Table 27.4).

and Nistor et al. (2017) conduct experiments regarding the entrainment of shipping containers at a scale of 1:40, where the focus is on the transport pattern of multiple arranged bodies due to bore impact.

Hansom et al. (2008) investigate cliff-top erosion and deposition of boulders by storm waves by simulating prototype coastal settings of the northern and western British Isles with steep cliffs, concluding that storm waves have a high capacity of moving cliff-top boulders.

Cytrynbaum (2018) and Cox et al. (2019) study boulder transport driven by storm waves at a scale of 1:100. The bathymetry and the shore are designed following the shape of the coastline of their prototype site on the Aran Islands off the western coast of Ireland (Cox et al., 2018). The authors find that, in agreement with field observations, even very large boulders can be transported by storm waves, even though specific constraints regarding the wave, boulder, as well as coastal topography and bathymetry are required.

Becker et al. (2015) investigate the behavior of pebbles in a flume, where channelized flow under fluvial conditions is simulated. In the same flume and with similar conceptual background, Gronz et al. (2016) test the application of a Smartstone probe, a new IMU, which is installed inside the clasts and tracks their movement in running water. However, comparing the movement patterns derived from Smartstones with high-speed camera tracking still reveals significant deviation in orientation and the clipping of data, which the authors hope to reduce in the future through the application of probabilistic modeling (Gronz et al., 2016).

Further experiments investigate the interactions between tsunamis and immovable solid bodies (e.g., coastal defense structures). Such experiments target the flow behavior of tsunamis at the shore and around buildings (e.g., Esteban et al., 2017) or evaluate the impact force acting on tsunami-mitigation structures (e.g.,

Table 27.5 Key information from selected experimental studies on transport of rigid bodies under wave attack not in particular related to tsunami-induced boulder transport.

	Stolle et al. (2016); Nistor et al. (2017)	Hansom et al. (2008)	Cytrynbaum (2018); Cox et al. (2019)	Becker et al. (2015); Gronz et al. (2016)	Yao et al. (2014)
Motivation	Entrainment of shipping containers	Cliff-top erosion and deposition of boulders by storm waves	Boulder transport by storm waves	Pebble transport/ tracking in steady flow	Behavior of solid bodies lighter than water under the impact of solitary waves
Experimental setup	3D wave basin Solitary wave with an extended tail	Flume ($74 \times 4.6 \times 2.2$ m^3) Storm wave series and single bore	3D wave basin JONSWAP (Joint North Sea Wave Project) storm wave spectrum	Flume (l = 2.7, w = 0.265 m) Steady flow (1 m/s) under fluvial conditions	Flume (l = 34, w = 0.55 m) Solitary wave
Transported bodies	Multiple bodies (shipping container)	Boulder (long axis 1.5–3.2 m)	Pebbles and cobbles (density 1.6 g/cm^3 to 2.55 g/cm^3)	Pebbles, cobbles, and cuboids up to 16 cm	Cubes of polyethylene ($10 \times 5 \times 5$ mm^3)
Special features	Real-time locating system (RTLS) for debris tracking	Downscaled cliff	Bathymetry and the shore are designed following the shape of the coastline of a prototype site on the Aran Islands (W Ireland)	IMU sensor; integrating a triaxial accelerometer, a magnetometer, and a gyroscope, which is installed inside the clasts and tracks their movement in running water	

Continued

Table 27.5 Key information from selected experimental studies on transport of rigid bodies under wave attack not in particular related to tsunami-induced boulder transport.—*cont'd*

	Stolle et al. (2016); Nistor et al. (2017)	Hansom et al. (2008)	Cytrynbaum (2018); Cox et al. (2019)	Becker et al. (2015); Gronz et al. (2016)	Yao et al. (2014)
Key outcomes	Established a function describing the maximum inland transport distance and another one describing the spreading angle, depending on the amount of debris bodies Random behavior of single debris after bore impact Results corroborate in situ observations of tsunami-induced debris transport of Naito et al. (2014)	Storm waves are able to mobilize cliff-top boulders Advocate caution to associate boulders, which are not deposited in the impact range of normal wave activity, strictly to tsunamis	Even very large boulders can be transported by storm waves, even though specific constraints regarding the wave, boulder, as well as coastal topography and bathymetry are required Bore velocity, boulder dimension, and wave front slope in combination with wave height are considered main influencing parameters on boulder transport	Similar influence of the pebble size, shape, and pre-transport orientation on transport	Highly sensitive behavior of the bodies, which increases with energy of the incoming wave. If multiple bodies are arranged in a line, the maximum inundation distance decreases

Robertson et al., 2008; Chen et al., 2016). Yao et al. (2014) study the behavior of solid bodies lighter than water under the impact of solitary waves. Key findings of Yao et al. (2014) include the highly sensitive behavior of the bodies, which increases with energy of the incoming wave. Additionally, they find that if multiple bodies are arranged in a line, the maximum inundation distance decreases.

Link to numerical models

Physical laboratory experiments have two main goals: deriving (analytical) descriptions of processes and interaction of different parameters, and the development of well elaborated datasets with quantitative results as basis for numerical models (e.g., Imamura et al., 2008; Nandasena and Tanaka, 2013). In the latter case, the quantitative results of experiments are used for comparison with results obtained from a numerical model and for calibration, verification, and validation. In this sense, the parameters of a numerical model are adjusted to find the parameter combination, which generates the numerical results best fitting those of the physical experiments. In numerical models, such parameters may be the (artificial) viscosity of the fluid, the numerical treatment of roughness and turbulences, or the computational time step. After the successful calibration, the numerical model can be used for a known event and setting of boulder transport and investigation of parameters that might not be changeable in physical experiments (e.g., roughness). If the numerical model sufficiently reproduces results for such an event, it is validated, meaning that the program is able to reproduce events/setups (e.g., experimental results) for which it is not especially programmed (e.g., real-world bathymetry or initial tsunami/earthquake parameters). An overview for definitions of calibration, validation, and verification can be found in NASA (2008). Regarding tsunami models, several benchmark tests exist (e.g., Synolakis et al., 2007; NTHMP, 2012), which are used to verify a developed numerical tsunami model for operational use. Afterwards, the model can be applied to unknown or possible future events, by still considering several restrictions. For boulder transport, no benchmarks similar to those of Synolakis et al. (2007) and NTHMP (2012) exist so far.

Conclusions and recommendations

Experimental studies on tsunami-induced boulder transport in particular or focusing on adjacent research questions (e.g., the transport of shipping containers) give essential insights into tsunami-induced transport of rigid bodies in nearshore areas and, thus, help to reconstruct past tsunamis based on the characteristics and spatial distribution of coastal boulders.

The existing experiments also provide a basis for developing and testing numerical models. However, across the existing publications a certain sensitivity of the boulder transport processes within high-energy, turbulent flows becomes obvious. Experiments show divergent predominant transport modes (e.g., rolling and saltation

in Imamura et al., 2008 and sliding in Liu et al., 2015) for different setups and especially the boulder's FI. The studies of Nandasena and Tanaka (2013) and Imamura et al. (2008) indicate that boulders with an FI ~ 1 are more likely transported by rolling compared to boulders with higher FI, while overall the predominant transport mode seems to be sliding (e.g., Freund, 2014; Liu et al., 2015; Nistor et al., 2017). However, the transport mode is highly influenced by the boulder shape, and since most published experiments use regular-shaped cuboids and cubes with different FIs, it needs to be investigated further in which amount more irregular shapes influence the transport mode. Oetjen et al. (2017, 2018) apply a boulder resembling a natural prototype and found sliding as the predominant transport mode as well, which is possibly related to the high FI. The influence on bottom roughness on transport mode, however, is not yet clear and needs to be addressed in future studies.

In general, authors agree that boulders tend to align the long axis parallel to the flow. Nandasena and Tanaka (2013) find shorter transport distances for high FI compared to cubic boulders, a hypothesis that is not yet confirmed by others.

For future studies, it would be beneficial if researchers agree on a basic set of parameters regarding their experimental setup, which should be clearly presented in publications (Table 27.6) and unequivocally defined. Equal terms for the boulder transport distance, for example, should be used throughout the research community. As in Imamura et al. (2008) the transport distance should at least be separated regarding the maximum transport distance and total transport distance (Fig. 27.9). An additional benefit might be to itemize boulder movements in direction components (e.g., in flow direction as well as perpendicular movements) in the result presentation. Regarding the bore, for example, a standardized point of velocity measurement with a fixed distance from the shore or boulder should be commonly used.

Table 27.6 Recommendation for standard parameters to be published with every experimental study.

Bore	Boulder	Transport process
Velocity	Density	Max. transport distance
Height	Dimensions	Total transport distance
Type of bore generation (e.g., dam break or piston system)	Shape	Mode
	Orientation	Time series
(Froude number)	Submergence	
	Flatness index (FI)	
	Scale (if applicable)	

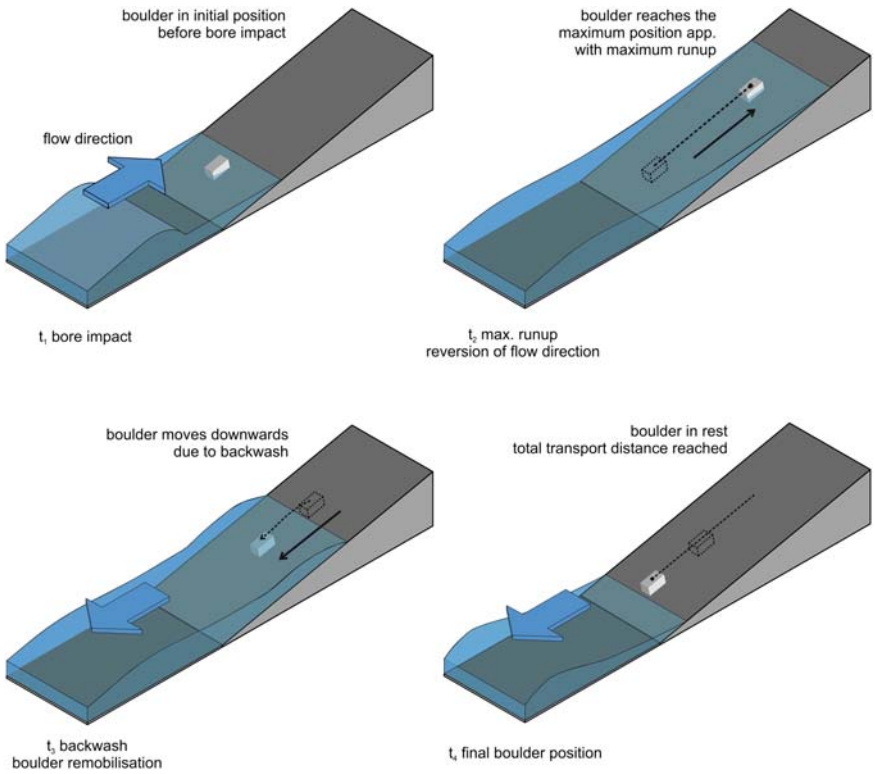

FIGURE 27.9

Difference of maximum transport distance and total transport distance for an initially partially submerged boulder setup (t_1). After the maximum flow runup (t_2) the boulder could be transported in backwash direction (t_3) before it finally comes to rest (t_4) possibly before the backwash ends on the initial water level.

The FI requires improvement to a general boulder index that considers shape and density. Due to the highly random boulder behavior under bore influence, it may even be advantageous to move a step back and to conduct very basic experiments (idealized shapes of different sizes, uniformly inclined channel, several wave heights) to better understand the basic processes. Existing experiments show sometimes diverging results leading to uncertain equations. For experiments focusing on boulder behavior, a standard wave bore could be defined facilitating the comparison of results from different studies with different boulder types. Vice versa, experiments focusing on the influence of wave parameters could benefit from standardized boulder models.

Focusing on the boulder shape, the step between two shapes should be as small as a divergent behavior between the shapes can be observed. This would help to find relationships between the boulder shape and transport behavior and could lead to

more reliable analytical equations and a stronger calibration basis for numerical models. Especially drag, lift, and friction forces are today considered as relatively widespread coefficients in numerical models and analytical solutions, which are commonly chosen according to observed and approximated values from literature and are not based on a fundamental understanding of the ongoing processes.

Even if numerical models provide a good alternative to physical experiments, they still suffer from physical inaccuracies (Chapters 28 and 29). Regarding tsunami-induced boulder transport, numerical models are at an early stage of development compared to more common questions in hydrodynamic research, and some crucial and basic mechanisms of nearshore tsunami hydrodynamics and the exerted forces are not entirely understood. Boulder transport experiments can provide answers to these questions and may help to improve not only specialized numerical boulder-transport models, but also numerical models focusing on the nearshore tsunami, its inundation extent, and especially the acting forces on coastal structures.

Acknowledgments

This contribution benefitted from funding by Deutsche Forschungsgemeinschaft (DFG) for the project "Modeling tsunami-induced coarse-clast transport − combination of physical experiments, advanced numerical modeling and field observations" (SCHU 1054/7-1, EN 977/3-1).

References

Allsop, W., Chandler, I., Zaccaria, M., 2014. Improvements in the physical modelling of tsunamis and their effects. In: Penchev, V., Taveira Pinto, F. (Eds.), Proceedings of the 5th International Conference Coastlab14 "Application of Physical Modelling to Port and Coastal Protection", Varna, Bulgaria, 29 September−2 October 2014. Black Sea−Danube Coastal Research Association (BDCA), Varna, pp. 3−22.

Bagnold, R.A., 1940. Beach formation by waves. Some Model Experiments in a wave tank. Journal of the Institution of Civil Engineers 15, 27−52. https://doi.org/10.1680/ijoti.1940.14279.

Becker, K., Gronz, O., Wirtz, S., Seeger, M., Brings, C., Iserloh, T., Casper, M.C., Ries, J.B., 2015. Characterization of complex pebble movement patterns in channel flow − a laboratory study. Cuadernos de Investigación Geográfica 41, 63−85. https://doi.org/10.18172/cig.2645.

Boesl, F., Engel, M., Eco, R.C., Galang, J.A., Gonzalo, L.A., Llanes, F., Quix, E., Brückner, H., 2019. Digital mapping of coastal boulders − high-resolution data acquisition to infer past and recent transport dynamics. Sedimentology. https://doi.org/10.1111/sed.12578.

Bressan, L., Guerrero, M., Antonini, A., Petruzzelli, V., Archetti, R., Lamberti, A., Tinti, S., 2018. A laboratory experiment on the incipient motion of boulders by high-energy coastal flows. Earth Surface Processes and Landforms 43, 2935−2947. https://doi.org/10.1002/esp.4461.

Buckingham, E., 1914. On physically similar systems; illustrations of the use of dimensional equations. Physical Review 4, 345−376. https://doi.org/10.1103/PhysRev.4.345.

Chanson, H., 2009. Current knowledge in hydraulic jumps and related phenomena. A survey of experimental results. European Journal of Mechanics - B: Fluids 28, 191−210. https://doi.org/10.1016/j.euromechflu.2008.06.004.

Chen, C., Melville, B.W., Nandasena, N.A.K., Shamseldin, A.Y., Wotherspoon, L., 2016. Experimental study of uplift loads due to tsunami bore impact on a wharf model. Coastal Engineering 117, 126−137. https://doi.org/10.1016/j.coastaleng.2016.08.001.

Cox, R., Jahn, K.L., Watkins, O.G., Cox, P., 2018. Extraordinary boulder transport by storm waves, and criteria for analysing coastal boulder deposits. Earth-Science Reviews 177, 623−636. https://doi.org/10.1016/j.earscirev.2017.12.014.

Cox, R., O'Boyle, L., Cytrynbaum, J., 2019. Imbricated coastal boulder deposits are formed by storm waves, and can preserve a long-term storminess record. Scientific Reports 9, 10784. https://doi.org/10.1038/s41598-019-47254-w.

Cytrynbaum, J., 2018. Can Storm Waves Move Very Large Boulders? Investigations in a Wave Tank (Bachelor thesis). Williams College, Williamstown, Massachusetts.

Esteban, M., Glasbergen, T., Takabatake, T., Hofland, B., Nishizaki, S., Nishida, Y., Stolle, J., Nistor, I., Bricker, J., Takagi, H., Shibayama, T., 2017. Overtopping of coastal structures by tsunami waves. Geosciences 7, 121. https://doi.org/10.3390/geosciences7040121.

Evers, F.M., 2018. Videometric water surface tracking of spatial impulse wave propagation. Journal of Visualization 21, 903−907. https://doi.org/10.1007/s12650-018-0507-1.

Fang, C., 2019. An Introduction to Fluid Mechanics. Springer, Cham. https://doi.org/10.1007/978-3-319-91821-1.

Freund, F., 2014. Experimentelle Untersuchung des boreninduzierten Transports von Gesteinsblockmodellen (Bachelor thesis). Technische Universität Braunschweig.

Gibbings, J.C., 2011. Dimensional Analysis. Springer, London. https://doi.org/10.1007/978-1-84996-317-6.

Goseberg, N., 2011. The run-up of long waves − laboratory-scaled geophysical reproduction and onshore interaction with macro-roughness elements. Mitteilungen des Franzius-Instituts für Wasserbau und Küsteningenieurwesen 97. https://doi.org/10.15488/7630.

Goseberg, N., 2012. A laboratory perspective of long wave generation. In: Proceedings of the 22nd International Offshore and Polar Engineering Conference, Rhodes, Greece, 17−22 June 2012. ISOPE-I-12-528.

Goseberg, N., Wurpts, A., Schlrumann, T., 2013. Laboratory-scale generation of tsunami and long waves. Coastal Engineering 79, 57−74. https://doi.org/10.1016/j.coastaleng.2013.04.006.

Goseberg, N., Stolle, J., Nistor, I., Shibayama, T., 2016. Experimental analysis of debris motion due to obstruction from fixed obstacles in tsunami-like flow conditions. Coastal Engineering 118, 35−49. https://doi.org/10.1016/j.coastaleng.2016.08.012.

Gronz, O., Hiller, P.H., Wirtz, S., Becker, K., Iserloh, T., Seeger, M., Brings, C., Aberle, J., Casper, M.C., Ries, J.B., 2016. Smartstones. A small 9-axis sensor implanted in stones to track their movements. Catena 142, 245−251. https://doi.org/10.1016/j.catena.2016.03.030.

Hansom, J.D., Barltrop, N.D.P., Hall, A.M., 2008. Modelling the processes of cliff-top erosion and deposition under extreme storm waves. Marine Geology 253, 36−50. https://doi.org/10.1016/j.margeo.2008.02.015.

Heller, V., 2011. Scale effects in physical hydraulic engineering models. Journal of Hydraulic Research 49, 293−306. https://doi.org/10.1080/00221686.2011.578914.

Herwig, H., 2008. Strömungsmechanik - Einführung in die Physik von technischen Strömungen. Vieweg+Teubner Verlag, Wiesbaden. https://doi.org/10.1007/978-3-8348-9497-7.

Hughes, S.A., 1993. Physical Models and Laboratory Techniques in Coastal Engineering. World Scientific, Singapore. https://doi.org/10.1142/2154.

Hsu, H.-C., Torres-Freyermuth, A., Hsu, T.-J., Hwung, H.-H., 2012. Numerical and experimental study of dam-break flood propagation and its implication to sediment erosion. Coastal Engineering Proceedings 33. https://doi.org/10.9753/icce.v33.sediment.7 sediment.7.

Imamura, F., Goto, K., Ohkubo, S., 2008. A numerical model for the transport of a boulder by tsunami. Journal of Geophysical Research 113, L24605. https://doi.org/10.1029/2007JC004170.

Kobus, H., 1974. Anwendung der Dimensionsanalyse in der experimentellen Forschung des Bauingenieurwesens. Bautechnik 3, 88−94. https://doi.org/10.18419/opus-8279.

Le Méhauté, B., 1976. An Introduction to Hydrodynamics and Water Waves. Springer, Berlin, Heidelberg. https://doi.org/10.1007/978-3-642-85567-2.

Li, Y., Chanson, H., 2017. Free-surface and velocity characteristics of tidal bore propagation against a slope: experiments on decelarating bores. In: Proceedings of 37th IAHR World Congress, Kuala Lumpur, Malaysia, 13−18 August 2017, vol. 4, Theme 4.3, pp. 3413−3422.

Liu, H., Sakashita, T., Sato, S., 2015. An Experimental study on the tsunami boulder movement. Coastal Engineering Proceedings 34, current.16. https://doi.org/10.9753/icce.v34.currents.16.

Liu, H., Liu, H., Guo, L., Lu, S., 2017. Experimental study on the dam-break hydrographs at the gate location. Journal of Ocean University of China 16, 697−702. https://doi.org/10.1007/s11802-017-3470-x.

Lloyd, T.O., 2016. An Experimental Investigation of Tsunami Forces on Coastal Structures. Ph.D. thesis. University College London.

Martin, H., Pohl, R., 2000. Technische Hydromechanik. Hydraulische und numerische Modelle. Verlag Bauwesen, Berlin.

May, S.M., Engel, M., Brill, D., Cuadra, C., Lagmay, A.M.F., Santiago, J., Suarez, K., Reyes, M., Brückner, H., 2015. Block and boulder transport in Eastern Samar (Philippines) during Supertyphoon Haiyan. Earth Surface Dynamics 3, 543−558. https://doi.org/10.5194/esurf-3-543-2015.

Munson, B.R., Young, D.F., Okiishi, T.H., Huebsch, W.W., 2009. Fundamentals of Fluid Mechanics. John Wiley & Sons, Hoboken.

Naito, C., Cercone, C., Riggs, H.R., Cox, D., 2014. Procedure for site assessment of the potential for tsunami debris impact. Journal of Waterway, Port, Coastal, and Ocean Engineering 140, 223−232. https://doi.org/10.1061/(ASCE)WW.1943-5460.0000222.

Nandasena, N.A.K., Tanaka, N., 2013. Boulder transport by high energy. Numerical model-fitting experimental observations. Ocean Engineering 57, 163−179. https://doi.org/10.1016/j.oceaneng.2012.09.012.

NASA, 2008. NPARC Alliance CFD Verification and Validation Web Site: Glossary of Verification and Validation Terms. https://www.grc.nasa.gov/www/wind/valid/tutorial/glossary.html (Accessed 23 January 2020).

Nistor, I., Goseberg, N., Stolle, J., Mikami, T., Shibayama, T., Nakamura, R., Matsuba, S., 2017. Experimental investigations of debris dynamics over a horizontal plane. Journal of Waterway, Port, Coastal, and Ocean Engineering 143, 4016022. https://doi.org/10.1061/(ASCE)WW.1943-5460.0000371.

NTHMP (National Tsunami Hazard Mitigation Program), 2012. Proceedings and Results of the 2011 NTHMP Model Benchmarking Workshop. U.S. Department of Commerce/ NOAA/NTHMP (NOAA Special Report), Boulder.

Oetjen, J., Engel, M., Pudasaini, S.P., Schüttrumpf, H., Brückner, H., 2017. An advanced three-phase physical, experimental and numerical method for tsunami induced boulder transport. Coastal Engineering Proceedings 35, management.4. https://doi.org/10.9753/icce.v35.management.4.

Oetjen, J., Engel, M., Schönberger, J.J., Pudasaini, S.P., Schüttrumpf, H., 2018. Simulation of boulder transport in a flume comparing cuboid and complex-shaped boulder models. Geophysical Research Abstracts 20. EGU2018-12124.

Rhinefrank, K., Schacher, A., Prudell, J., Stillinger, C., Naviaux, D., Brekken, T., von Jouanne, A., Newborn, D., Yim, S., Cox, D., 2010. High resolution wave tank testing of scaled wave energy devices. In: Proceedings of OMAE2010, 29th International Conference on Offshore Mechanics and Arctic Engineering 505−509. https://doi.org/10.1115/OMAE2010-20602.

Robertson, I.N., Riggs, H.R., Mohamed, A., 2008. Experimental results of tsunami bore forces on structures. In: Proceedings of the 27th International Conference on Offshore Mechanics and Arctic Engineering 509−517. https://doi.org/10.1115/OMAE2008-57525.

Robertson, I.N., Paczkowski, K., Riggs, H.R., Mohamed, A., 2011. Tsunami bore forces on walls. In: Proceedings of the 30th International Conference on Offshore Mechanics and Arctic Engineering 395−403. https://doi.org/10.1115/OMAE2011-49487.

Schimmels, S., Sriram, V., Didenkulova, I., 2016. Tsunami generation in a large scale experimental facility. Coastal Engineering 110, 32−41. https://doi.org/10.1016/j.coastaleng.2015.12.005.

She, Z.S., Leveque, E., 1994. Universal scaling laws in fully developed turbulence. Physical Review Letters 72, 336−339. https://doi.org/10.1103/PhysRevLett.72.336.

Spurk, J., Aksel, N., 2018. Strömungslehre. Einführung in die Theorie der Strömungen. Springer, Berlin. https://doi.org/10.1007/978-3-642-13143-1.

Stolle, J., Nistor, I., Goseberg, N., 2016. Optical tracking of floating shipping containers in a high-velocity flow. Coastal Engineering Journal 58, 1650005. https://doi.org/10.1142/S0578563416500054.

Strusińska-Correira, A., Hermann, A., Freund, N., Martins, K.A., Oumeraci, H., 2017. Transport characteristics of coarse clasts under tsunami-bore conditions based on large-scale model experiments. In: Costa, P.J.M., Andrade, C., Freitas, M.C. (Eds.), Abstract Volume of the 5th International Tsunami Field Symposium, Lisbon, Portugal, 3−7 September 2017, pp. 115−116.

Synolakis, C.E., Bernard, E.N., Titov, V.V., Kânoğlu, U., González, F.I., 2007. Standards, criteria, and procedures for NOAA evaluation of tsunami numerical models. NOAA Technical Memorandum OAR PMEL 135.

Tavoularis, S., 2006. Measurement in Fluid Mechanics. Cambridge University Press, Cambridge.

Yao, Y., Huang, Z., Lo, E.Y.M., Shen, H.-T., 2014. A preliminary laboratory study of motion of floating debris generated by solitary waves running up a beach. Journal of Earthquake and Tsunami 8, 1440006. https://doi.org/10.1142/S1793431114400065.

Yeh, H.H., 1991. Tsunami bore runup. Natural Hazards 4, 209−220. https://doi.org/10.1007/BF00162788.